A Comparison of the Fracture Behavior of Two Heats of the Secondary Hardening Steel AF1410

K. J. HANDERHAN, W. M. GARRISON, Jr., and N. R. MOODY

The fracture behavior of two heats of AF1410 steel has been investigated for two aging temperatures, 425 °C and 510 °C. The first heat, modified by deliberate lanthanum additions, contains lanthanum-rich inclusions characterized by an inclusion spacing of 7.6 μm. The second heat, not modified by lanthanum additions, contains a comparable volume fraction of much smaller CrS inclusions characterized by an inclusion spacing of 2.3 μm. Of the mechanical properties measured, only the toughness appears to be influenced by inclusion type. For example, on aging at 510 °C, δ_{IC}, the critical value of the crack tip opening displacement, for the lanthanum modified heat is 66 μm compared to 28 μm for the heat containing CrS inclusions. This influence of inclusion type is attributed to the larger spacing of the inclusions in the lanthanum modified heat. In addition, for both heats the toughness on aging at 510 °C was higher than after aging at 425 °C. Particle analysis from extraction replicas of polished cross-sections of as-quenched materials and of fracture surfaces of the 425 °C and 510 °C microstructures indicates that on aging at 510 °C only undissolved particles inherited from the austenitizing temperature nucleate secondary voids, but that on aging at 425 °C carbides precipitated on aging nucleate secondary voids as well.

I. INTRODUCTION

THE fracture initiation toughness of ultra high strength steels can be influenced by the inclusion type and spacing, the microstructural parameters established during austenitizing, and how the microstructure evolves during aging or tempering. The theoretical treatment of Rice and Johnson[1] suggests that the critical value of the crack tip opening displacement, δ_{IC}, will scale with the inclusion spacing, X_0, at least over some range of X_0. This prediction appears to be in accordance with experimental studies,[2,3] at least as long as certain requirements are met. These requirements appear to include that the inclusions can be regarded as pre-existing voids and that the microstructure remains otherwise constant. The austenitizing treatment will, for a given alloy composition, largely determine the characteristics of the undissolved particles (such as undissolved carbides) and the prior austenite grain size. These undissolved particles can affect the fracture behavior directly if they actually nucleate voids and indirectly through their influence on prior austenite grain size. Aging can influence the fracture behavior directly if particles precipitated on aging nucleate voids and indirectly by altering the flow characteristics of the matrix.

The work of Speich *et al.*[4] provides an example of how, by control of composition and aging temperature, microstructures with very high toughness can be obtained. Explicitly it was shown that microstructures achieved by replacing cementite with very fine dispersions of alloy carbides precipitated during aging possess extremely high levels of toughness. It was suggested that the high toughness was possible because the fine alloy carbides were too small to nucleate voids. This work led to the development of HY180 steel (0.11C/10Ni/8Co/2Cr/1Mo), in which the alloy carbides precipitated on aging are M_2C type carbides where the M is Cr and Mo. Cobalt additions were used to enhance the secondary hardening strengthening. The carbon, chromium, and molybdenum levels are such that on aging at 510 °C only fine alloy carbides are precipitated. At this aging temperature yield strengths of 1250 MPa and fracture toughnesses of over 200 MPa$\sqrt{m}$ have been achieved. This basic microstructure has been exploited in the development of the steel AF1410,[5,6] which is identical to HY180 except for increased carbon and cobalt contents (0.16C and 14Co). The increased cobalt is used to enhance further the secondary hardening reaction. This steel is presently commercially available and on aging at 510 °C yield strengths of 1550 MPa and fracture toughnesses of over 200 MPa$\sqrt{m}$ have been achieved.

In an earlier study[7] of a commercially produced heat of AF1410, it was found that lanthanum additions had been made so that the inclusions in the steel were not MnS or CrS. Instead, the inclusions were rich in La and in most cases S. Based on the expected sequence[8,9] of inclusion formation in La treated steels, these inclusions were probably La oxides and La oxy-sulfides. The inclusion volume fraction was comparable to those of steels of similar sulfur levels in which the inclusions are MnS. However, the inclusions in the La modified heat of AF1410 were much larger and more widely spaced than the MnS inclusions in steels produced by a vacuum induction melting and subsequent vacuum arc remelting (VIM/VAR) practice.[3,10] It was concluded on the basis of previous studies of low alloy ultra high strength steels that the high fracture toughness of the commercially produced AF1410 could be partially attributed to the relatively large inclusion spacing. Further, it was predicted that if the La-rich inclusions were replaced by the same volume fraction of inclusions of the smaller size and spacing as normally encountered in VIM/VAR materials, the fracture toughness of AF1410 aged at 510 °C would decrease to about 130 MPa$\sqrt{m}$.

The purpose of this present work was to compare the fracture behavior of two heats of AF1410. One heat has been modified by La additions and is characterized by an inclusion spacing of about 7.6 μm. No deliberate

K. J. HANDERHAN is Vice President of Technology, Ellwood City Forge, Ellwood City, PA. W. M. GARRISON, Jr. is Associate Professor, Department of Metallurgical Engineering and Materials Science, Carnegie Mellon University, Pittsburgh, PA 15213. N. R. MOODY is Member, Technical Staff, Sandia National Laboratories, Livermore, CA 94550.

Manuscript submitted July 8, 1988.

lanthanum additions were made to the second heat; the inclusions in this second heat were CrS at a spacing of 2.3 μm. The mechanical properties of both heats were assessed after aging at 425 °C, the aging temperature of lowest toughness (see Figure 3), and after the commercial aging treatment of 510 °C. Thus the influence of inclusion type and spacing on the fracture behavior was assessed for two different microstructures. In addition, to determine the extent to which changing the aging temperature directly influenced the fracture behavior, the types and size distributions of carbides inherited from the austenitizing treatment were determined from extraction replicas of polished cross-sections of asquenched material and these results compared to those obtained from extraction replicas of fracture surfaces for both the 425 °C and 510 °C microstructures. The data on inclusion spacing and fracture initiation toughness have been summarized previously.[11]

II. EXPERIMENTAL PROCEDURE

A. *Materials and Processing*

Material from two heats of AF1410 were evaluated. The first heat (heat 1) was melted by Cytemp, employing a lanthanum addition during vacuum induction melting to modify inclusion type. The second heat (heat 2), prepared by Teledyne Allvac, was also vacuum induction melted although no deliberate lanthanum additions were made. Both heats were vacuum arc remelted prior to forging. The ingots were forged to blooms and subsequently rolled to 114 mm diameter round bar. Initial hot working was performed at 1175 °C with final hot working begun at approximately 980 °C with finishing temperatures below 870 °C. All bars were supplied in the normalized (900 °C–6 hours–air cool) and overaged conditions (680 °C–6 hours–air cool), as specified in AMS 6427.[12] The compositions of both heats after vacuum arc remelting are given in Table I. Note the La content of heat 1 was 0.008 wt pct and that of heat 2 was less than 0.002 wt pct.

Oversized specimen blanks for all mechanical tests were cut from the as-received bars prior to heat treatment. All specimens were oriented such that the axis of load application was in the principal hot working direction (longitudinal direction) and crack propagation was in the transverse direction (L-T orientation). All specimens were first held at 899 °C for 1 hour and then air cooled, austenitized at 823 °C for 1 hour and oil quenched, followed by aging at either 425 °C or 510 °C for five hours. After aging, all samples were water quenched. Austenitizing was carried out in a vertical tube furnace under flowing argon, and aging treatments were conducted in neutral salt baths.

B. *Mechanical Properties*

The mechanical properties determined were smooth axisymmetric tensile properties, plane strain tensile properties, the Charpy impact energy, and the fracture initiation toughness.

Standard 6.4 mm round tensile specimens with a 25 mm gage length were utilized to determine conventional tensile properties such as yield strength, ultimate tensile strength, elongation (pct el.), reduction in area (pct RA), and fracture stress, in accordance with ASTM E8.[13] Loads at 0.2 pct offset displacement were used to calculate yield strength values. Specimen surfaces were prepared by grinding the gage length region with 600 grit SiC paper after machining. Initial gage lengths were marked on the specimens using calibrated one-inch punch marks. Tensile tests were conducted at room temperature using an Instron model 1125 screw driven machine at a crosshead speed of 0.5 mm/min. Specimen displacement was continuously measured up to and slightly past maximum load, using a strain gage extensometer. In addition to conventional strength and ductility measurements, strain hardening exponents were calculated by assuming a simple power law behavior for post yield deformation, as described in ASTM E646.[14] True stress and true plastic strain data from approximately the proportional limit to the point of maximum load were used in the calculation of the strain hardening exponent.

The dimensions of the plane strain tensile specimens utilized in this study are illustrated in Figure 1. These specimens were similar to those first reported by Corrigan *et al.*,[15] in that $w/B/t$ was in the ratio of 30/3/1, where w = width of the reduced section, B = length of the reduced section, and t = thickness of the reduced section. Corrigan *et al.*,[15] by measuring strain patterns on gridded specimens, demonstrated that these conditions are necessary to insure full plane strain constraint and subsequent elevation of yield strength, as expected from the Von Mises yield criterion. The design of this specimen provides a higher degree of constraint than the Clausing type specimen[16,17] often utilized by other investigators.[18,19]

Experimental observations by Clausing[16,17] and the theoretical considerations of Tvergaard *et al.*,[20] dealing with surface imperfections, which might simulate grinding lines, suggest that plane strain ductility may be affected by the specimen surface condition. For this reason, both surfaces of the reduced section were carefully prepared prior to testing to insure that only microstructural influences on plane strain ductility were measured. Both sides of the reduced section were sequentially ground with 240, 320, 400, and 600 grit SiC papers fastened to a steel block of slightly smaller dimension than the length of this section. After grinding, these surfaces were polished with 6 μm and 1 μm diamond paste using a nylon polishing cloth fastened to the same steel block. These surfaces resembled typical metallographic specimens after completion of this procedure. Prior to testing, the thickness of the reduced section of each specimen was measured with a knife edge micrometer at five places along the width of the specimen. The initial thickness of the specimen was considered to be the average of these measurements.

Table I. Compositions of Two Heats of AF1410*

Alloy	C	Co	Ni	Cr	Mo	V	Mn	P	S	Si	Al	O	N	La
Heat 1 (La)	0.16	14	10.1	2.1	1.0	0.001	0.03	0.004	0.001	0.03	0.003	0.0009	0.0003	0.008
Heat 2	0.16	14	9.97	2.04	1.0	0.001	0.001	0.004	0.001	0.01	0.003	0.001	0.0009	<0.002

*Compositions in wt pct; O and N are total.

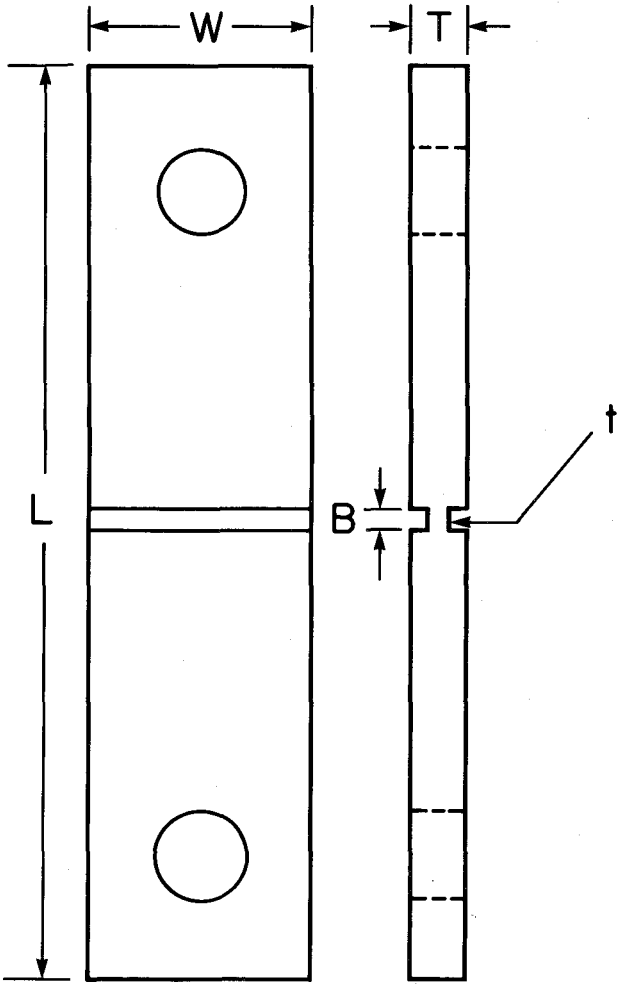

Fig. 1—A schematic of the plane strain tensile specimen used in this study.

Plane strain tensile specimens were pin loaded and pulled to fracture at a displacement rate of 0.1 mm/min in either a 10,000 kg screw driven Instron tensile testing machine or in a 50 kip MTS servohydraulic test frame. A diametral extensometer equipped with specially machined, adjustable, needle-point contact arms was used to monitor thickness contraction during the test. Plots of load *vs* thickness contraction were obtained until fracture as the diametral strain gage was not removed prior to fracture. Yield strength (0.2 pct offset) and ultimate tensile strength data plane strain were obtained from these tests. In addition, the plane strain ductility was determined from the following expression:[16]

$$\varepsilon_{f,PS} = \ln(t_0/t_f) \qquad [1]$$

where t_0 = initial thickness of reduced section and t_f = final thickness of reduced section. The final thickness was determined by viewing the fracture face of the specimen along the tensile axis in a traveling microscope and measuring the projection of the minimum dimension. The final thickness values were the averages of traveling microscope measurements over the central 75 pct of the width of the reduced section. The measurements were limited to this central region since Anand and Spitzig[19] have demonstrated that it is in this region that plane strain conditions are assured to exist.

Impact toughness values were measured at room temperature using the standard blunt notch Charpy V-notch specimen in accordance with ASTM E23.[21] Duplicate specimens were tested for the microstructures investigated. A Baldwin 240 ft.-lb. impact testing machine was used.

Fracture initiation toughness levels were determined by the J-integral fracture toughness test method according to ASTM E813-81,[22] using the single specimen unloading compliance method.[23] Compact tension specimens without side grooves were used. All tests were performed in a 50 kip MTS servohydraulic closed loop testing system. After precracking in accordance with ASTM E813-81,[22] specimens were loaded under stroke control at a displacement rate of 0.5 mm/min. Load and load-point displacement were continuously recorded during the test. Load-point displacement was measured using an extended arm displacement gage attached to razor blades which were fastened to the specimen at the load line using Superglue brand adhesive. During testing, the specimens were partially unloaded by an amount never exceeding 15 pct of the current load at intervals of approximately 0.05 to 0.10 mm (0.002 to 0.004 in.) crack mouth opening displacement. The unloading portion of the load-deflection curves was magnified $\approx 10\times$ using a zero suppression circuit and recorded autographically on a separate X-Y recorder. Unloading compliance slopes were obtained from these curves. Crack lengths were estimated from the compliance calibration relationship provided by Saxena and Hudak.[24] Special flat bottomed clevis grips, as described in ASTM E813-81,[22] were utilized in an attempt to minimize the hysteresis loop generated during this unloading-reloading sequence. The resultant magnified unloading slopes were generated with minimal hysteresis. Tests were stopped after each specimen exhibited approximately 1.52 mm (0.060 in.) of stable crack growth as estimated by the compliance technique. The accuracy of the compliance measurement system was confirmed for at least one specimen from each material and heat treatment condition by heat tinting the actual physical crack extension. This involved heating the specimens to 350 °C for thirty minutes prior to fracturing them open at a rapid rate in the MTS machine. In all cases, reported J_{IC} values corresponded to tests in which measured changes in physical crack length agreed with values estimated from compliance measurements within 15 pct. In addition, initial fatigue crack lengths estimated from the compliance measurements agreed with the actual fatigue crack lengths within 5 pct in all cases. J values were calculated using the modified Merkle-Corten[25] relationship, and J values were not corrected for crack growth. Graphical integration methods were used to measure the area under load-deflection curves. All J_{IC} values reported are based on linear regression analysis of J-Δa points within the exclusion lines defined in ASTM E813-81.

C. *Microstructural Examination*

All specimens for light and electron metallography were cut from fractured J_{IC} or Charpy impact specimens. Samples for microstructural and second phase particle characterization at both the optical and scanning electron (SEM) level were mounted in blue diallyl phthalate mounting material and prepared by sequential grinding through 120, 240, 320, 400, and 600 grit silicon carbide papers followed

by 6 μm and 1 μm diamond polishing compounds on nylon polishing cloth. The time spent during polishing with diamond paste was limited to approximately one minute during each step. Final preparation consisted of a brief polish ($\approx$15 to 20 seconds) using 0.06 μm silica (Buehler Mastermet solution) on a low nap Buehler Chemomet cloth. This procedure resulted in almost complete retention of nonmetallic inclusions. All polished specimens which were examined in the SEM were made conductive by applying copper tape across the specimens and further enhancing contact with silver paint.

The microstructures were examined optically in both the longitudinal and transverse planes after etching in Vilella's reagent[26] using a Reichert Ultrastar metallograph. Here, the longitudinal plane is defined as the plane whose normal is parallel to the principal hot working direction while a transverse plane is characterized by a normal which coincides with the transverse direction with respect to hot working. The extent of microstructural banding was characterized. In addition, prior austenite grain size measurements were obtained from polished longitudinal specimens after etching in a 4 pct picral solution in methanol containing a few drops of zepherin chloride as a wetting agent. Linear intercept grain sizes were determined according to ASTM E112[27] using the Hilliard circle method. A minimum of ten fields was examined for the grain size determinations.

The retained austenite levels present after heat treatment for all of the materials and heat treatment conditions tested were determined by the direct comparison X-ray technique developed by Averbach and Cohen[28] as modified by Miller.[29] Measurements were made using molybdenum radiation with a Rigaku X-ray diffractometer, operating at 40 kV and 20 mA and a scanning rate of 0.2 deg/minute. Flat specimens were prepared in the same manner as for the specimens for metallography. However, the specimen surface was etched and repolished with 0.06 μm silica three times in an attempt to eliminate surface effects due to stress induced transformation of austenite.

D. *Second Phase Particle Characterization*

Average nonmetallic inclusion radii and volume fractions were measured for each material. Plane polished specimens prepared in the manner described in Section C were examined in a Camscan series 4 scanning electron microscope equipped with a backscattered electron detector and a PGT System 4 energy dispersive X-ray spectrometer. Measurements were obtained from as-quenched samples for all materials to avoid the possibility of imaging larger tempered carbide particles. The transverse plane was used for all measurements. To insure that results were not substantially affected by inclusion shape, confirming measurements were performed for each heat in at least one heat treatment condition on a longitudinal plane. Measurements of the apparent diameters of at least 150 inclusion particles were obtained for both materials from random SEM backscattered electron micrographs at a magnification of 2000$\times$ for heat 1 and 4000$\times$ for heat 2. The chemical compositions of approximately twenty particles from every sample examined were qualitatively determined by energy dispersive methods.

In addition to the characterization of nonmetallic inclusion particles, the characteristics of additional undissolved particles were examined through the use of carbon extraction replicas of polished cross-sections. Only the as-quenched conditions were examined so that only particles present during a given austenitizing treatment or formed during cooling from these treatments would be captured. Single stage carbon extraction replicas were prepared from specimens that were etched for 3 minutes in 5 pct HNO_3 in ethanol after first being polished to 1 μm diamond and cleaned several times with cellulose acetate replica tape. Etched specimens were shadowed at $\approx$15 deg with Pt-C followed by vertical deposition of a thin ($\approx$700 to 1000 Å) layer of carbon. Shadowed replicas were utilized in an effort to assess extraction efficiency, as suggested by Stumpf and Sellars.[30] The coated surfaces were scribed with a razor blade into 2 mm squares and the replicas were etched free in 10 pct HNO_3 in ethanol. These carbon films were then captured on 200 mesh copper grids and washed in a series of three ethanol rinses and one distilled water rinse. Replicas were examined in a JEOL 200CX TEM operating at 120 KV. Particle size distributions were obtained from particle size measurements performed on 33,000X TEM bright-field micrographs. A number of the extracted particles were analyzed for chemical composition using the Scanning Transmission Electron Microscope (STEM) feature available on the Phillips 400 TEM in conjunction with a PGT series 4 EDS system or by simply converging the beam onto a particle and performing the microanalysis. EDS analysis was complicated by peak overlap due to the Pt shadowing. Therefore, additional samples not shadowed with Pt were examined. In addition, an attempt was made to estimate the volume fraction of the second phase particles extracted in this manner using the following expression:[30]

$$f = \alpha \cdot N \cdot (\bar{x}^2 + \sigma^2)$$

where f = volume fraction,
$\alpha = \pi/6$ for the case of perfect extraction efficiency,
N = number of particles per unit area obtained from lightly etched specimens,
$\bar{x}$ = arithmetic mean of particle distribution from heavily etched specimens,
σ = standard deviation of particle size distribution obtained from heavily etched specimens.

It must be remembered that estimates of volume fraction from extraction replicas are subject to wide variations due to errors in assessing extraction efficiency, particle sectioning effects, and assuring complete extraction of the entire particle size distribution.[31]

E. *Fractographic Characterization*

The fracture surfaces of the J_{IC} specimens for each material and heat treatment evaluated were qualitatively examined in the Camscan Series 4 SEM. For more quantitative evaluation, random fractographs were taken at various magnifications, depending on the relative scale of void sizes present, to quantitatively determine void sizes and the size of particles associated with these voids. All fractographs were taken within a distance of 2 to 3 times the value of the critical crack tip opening displacement in the crack growth direction and near the mid-thickness of the specimen. Void size distributions as viewed normal to the macroscopic fracture plane for those voids containing resolvable particles were determined from the fractographs.

A minimum of 300 voids containing particles was measured. In addition to the measurement of void size distributions for voids containing particles, the overall average projected linear intercept void size was determined for all materials and heat treatments. This was accomplished in the same manner as described for prior austenite grain size measurements.

In addition to fracture surface examination in the SEM, fracture surface extraction replicas were examined in the TEM to determine the nature of void nucleating particles which could not be resolved in the SEM. Freshly broken CVN specimens were first shadowed at 45 deg in the crack growth direction with Pt-C followed by vertical deposition of a heavy layer of carbon. Again, Pt shadowing complicated particle identification on the fracture surface replicas and was therefore eliminated from the procedure. These replicas were otherwise prepared for examination on the JEOL 200CX or Phillips 420 TEM by the same procedure described above for the plane polished extraction replicas.

III. RESULTS

A. *Mechanical Properties*

The axisymmetric tensile properties for both lots of material are presented in Table II. All mechanical property values listed are the average of a minimum of two tests. Note that the strength and ductility of these two heats were very similar for a given aging treatment. For a given heat of AF1410, increasing the aging temperature from 425 °C to 510 °C resulted in an increase in the 0.2 pct offset yield strength but a decrease in the ultimate tensile strength concurrent with a decrease in the strain hardening exponent. However, the flow stress σ_0, defined as the average of the yield and ultimate strengths, was practically independent of aging temperature for both heats. In addition, the ductility as measured by the pct elongation and pct RA increased modestly with increasing aging temperature. These results are very similar to those reported in the literature[7,32] for this secondary hardening steel heat treated in a similar manner.

The plane strain tensile properties of both heats were also very similar for a given aging treatment (see Table III). Consistent with the theoretical elevation of yield strength for a Von Mises material in plane strain, both the yield and the ultimate tensile strengths were elevated in plane strain for a given aging condition. This elevation in strength level for each material was approximately 12 pct compared to the theoretically expected increase of 15 pct and was similar to the values reported by Corrigan *et al.*[15] for a variety of ultra-high strength steels. It should be noted that the plane strain ductility appeared to be more sensitive to aging temperature than the axisymmetric ductility. The ratios of axisymmetric fracture strain to plane strain tensile ductility were much less than the 0.25 value reported by Clausing[16] and Speich and Spitzig[33] for materials of similar tensile strength. The work hardening exponent in plane strain was lower than the axisymmetric work hardening exponent in all cases. Wagoner[34] noted similar behavior in 2036-T4 aluminum.

Blunt notch Charpy impact energies for each heat and heat treatment condition are listed in Table III. Although the Charpy impact energy of the 425 °C aging condition was similar for the two heats, the Charpy impact toughness of the La treated heat was considerably higher (heat 1–88 J) than the untreated heat (heat 2–61 J) after aging at 510 °C.

J_{IC} values are given in Table IV. K_{IC} values (K_Q for heat 1 aged at 425 °C) were determined for the 425 °C condition of both heats since these specimens exhibited pop-in behavior, making it impossible to perform J-integral testing. In

Table II. Smooth Axisymmetric Tensile Properties

Condition	UTS (MPa)	0.2 Pct Offset YS (MPa)	Flow Stress (MPa)*	Pct Elong.	Pct RA	Fracture Strain**	Fracture Stress (MPa)***	n
425 °C								
Heat 1	1749	1354	1552	16.0	61.7	0.96	2878	0.12
Heat 2	1757	1398	1578	12.0	60.7	0.94	2851	0.11
510 °C								
Heat 1	1659	1503	1581	16.5	68.5	1.16	3028	0.09
Heat 2	1699	1527	1613	18.0	68.5	1.16	3002	0.08

* Flow stress = 0.5 (UTS + YS).
** $\ln(A_f/A_0)$.
*** Fracture stress not corrected for triaxiality due to necking.

Table III. Plane Strain Tensile Properties and Charpy Impact Energies

Condition	UTS (MPa)	0.2 Pct Offset YS (MPa)	Fracture Strain	Strain Hardening Exp.	CVN @ 25 °C (Joules)
425 °C					
Heat 1	1965	1583	0.13	0.07	30
Heat 2	1988	1600	0.14	0.09	28
510 °C					
Heat 1	1868	1715	0.20	0.05	88
Heat 2	1866	1658	0.18	0.07	61

Table IV. Fracture Initiation Toughness

Condition	J_{IC} (MPa-m)	K_{IC} or K_{IJ} (MPa$\sqrt{m}$)	σ_0 (MPa)	n	d_n	δ_{IC} (μm)**
425 °C						
Heat 1	—	118.5*	1552	0.12	0.56	22.8
Heat 2	—	86.2	1578	0.11	0.56	12.0
510 °C						
Heat 1	0.177	196.6	1581	0.09	0.60	66.3
Heat 2	0.075	128.2	1613	0.08	0.60	27.9

* K_Q value.
** δ_{IC} calculated from $\delta_{IC} = d_n J_{IC}/\sigma_0$ using Shih's values for d_n.[48]

addition, K_{IJ} values, *i.e.*, K_{IC} values computed from J_{IC} values, are also provided in Table IV. Values of the critical crack tip opening displacement, δ_{IC}, were computed from these data for the appropriate flow strengths and work hardening exponents for these materials. Note that the fracture toughness of the rare earth treated steel was significantly better than the untreated heat at both aging conditions investigated. Heat 1 exhibited a calculated value of δ_{IC} of 22.8 μm and 66.3 μm for the 425 °C and 510 °C aging treatments, respectively, compared to 12 μm and 27.9 μm for the second heat at the same aging treatments.

B. *Microstructural Characterization*

Based on the known hardenability of this alloy[32] and the estimated cooling rates (≈20 °C/sec) experienced by the fracture toughness specimens during quenching, the microstructures would be expected to be fully martensitic after oil quenching except for some retained austenite.[32] The prior austenite grain size was found to be the same in both heats (14 μm ± 1.0 μm @ 95 pct confidence level). Examination of the martensite packet structure at higher magnifications in the SEM revealed that the lath packet sizes were between 6 and 10 μm.

Optical examination of both heats of AF1410 revealed the presence of considerable microstructural banding, as illustrated in Figure 2. These banded regions appeared dark after etching and apparently resulted from the interdendritic segregation of elements such as C, Ni, Mo, and possibly Mn, as has been found for maraging steels.[35] AF1410 is more similar to maraging steels than standard low alloy ultra-high strength steels.

The effect of aging temperature on retained austenite content and its mechanical stability were determined using a La modified heat investigated earlier.[7] These results (Figure 3) show that the retained austenite is about 6 pct in the as-quenched condition and decreases with increasing aging temperature until it reaches a minimum of about 1 pct after aging at 475 °C. The retained austenite contents on aging at 510 °C and 550 °C were about 1.5 pct. X-ray diffraction was used to determine the retained austenite contents as a function of aging treatment for both heats examined in the present study. Both heats exhibited the same retained austenite levels for a given aging treatment. These results were consistent with the results given in Figure 3 and are summarized in Table V.

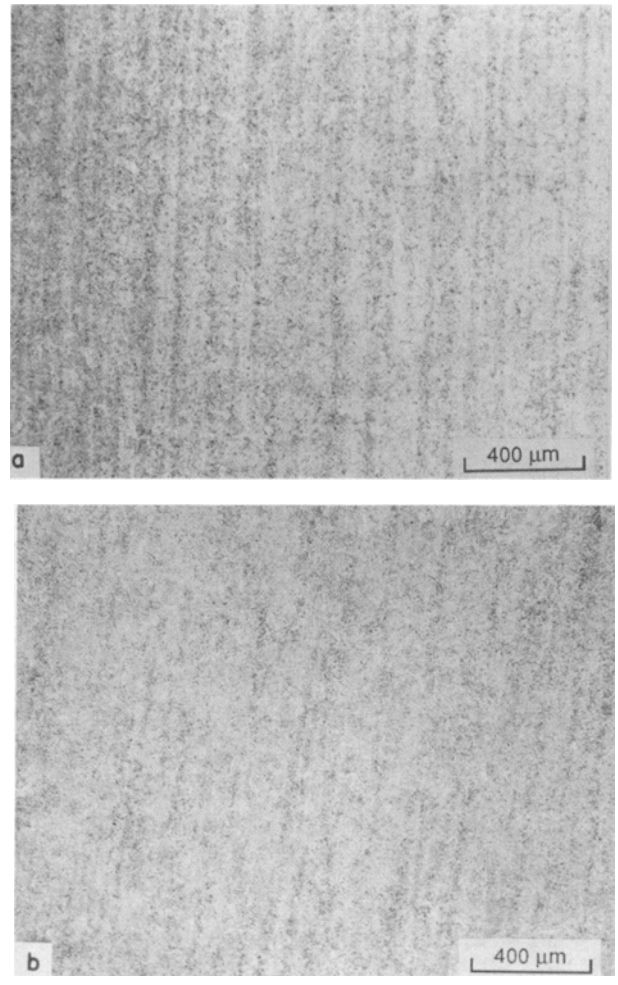

Fig. 2—Microstructural banding in AF1410 for (*a*) heat 1 and (*b*) heat 2.

C. *Bulk Second Phase Particle Characterization*

Based on the low sulfur (≈10 ppm) and total product oxygen contents (≈10 ppm) of these heats, both were expected to be very clean from a nonmetallic inclusion standpoint. In fact, it was difficult to resolve by light microscopy the inclusion particles in heat 2. However, in heat 1, light microscopy revealed strings of individual, nearly spherical particles on the T-plane (*i.e.*, plane parallel to the hot

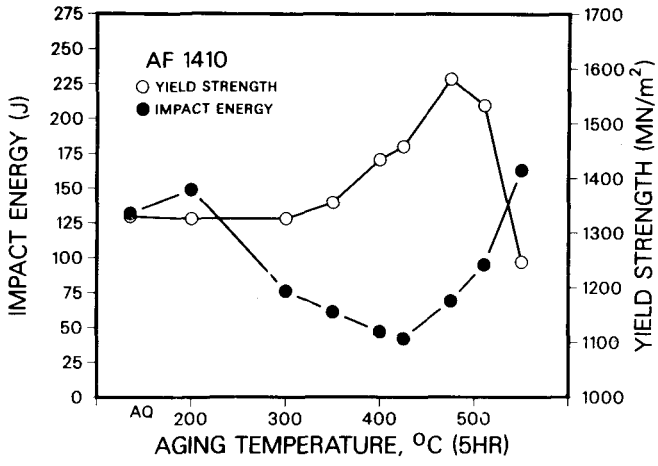

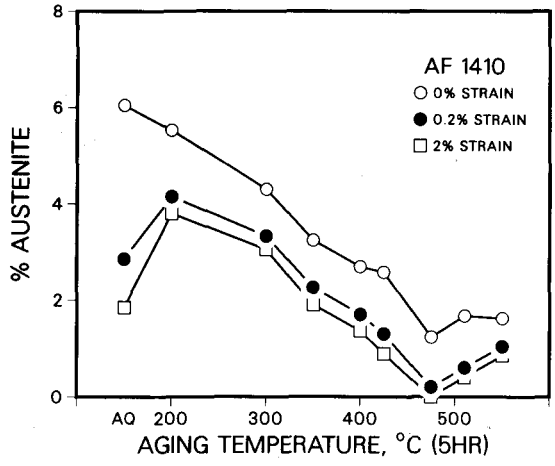

Fig. 3—The Charpy impact energy, yield strength, and vol pct austenite levels of AF1410 plotted as a function of aging temperature. The curve for 0 pct strain is the amount of austenite after aging. The curves for 0.2 pct and 2 pct strain indicate the amount of austenite when the material is strained to these levels. Retained austenite measurements were by a magnetic saturation technique.[49]

Table V. Retained Austenite Measurements

Material	Aging Temperature (°C)	Vol. Fraction Retained Austenite
Heat 1	425–5 hours	2.0 pct
Heat 2	425–5 hours	2.2 pct
Heat 1	510–5 hours	1.2 pct
Heat 2	510–5 hours	1.0 pct

working direction), as illustrated in Figure 4. These strings of particles were very widely spaced (≈300 to 400 μm) in the short transverse direction and were normally located within the dark etching microstructural bands or at the interface between the light and dark etching regions. Particles within the strings were generally much larger (≈4 to 10 μm diameter) than the average inclusion size. Very few such strings were observed in heat 2, and those present were even more widely spaced (≈1000 μm) than those in heat 1.

The inclusion volume fraction and average inclusion size were determined from measurements made on random 2000× SEM micrographs for heat 1 and 4000× micrographs for heat 2. A higher magnification was used for heat 2 because of the much smaller inclusion size. Typical inclusions for each heat were nearly spherical in all cases, with an average apparent aspect ratio of 1.08 for heat 1 and 1.03 for heat 2. Average true inclusion radii, R_0, were determined from the apparent inclusion diameters using the expression $R_0 = \pi/4 \cdot H(D)$[36] where $H(D)$ is the harmonic mean of the apparent diameter (D). Average three-dimensional nearest neighbor inclusion spacings (X_0) were obtained from the following relationship:[31]

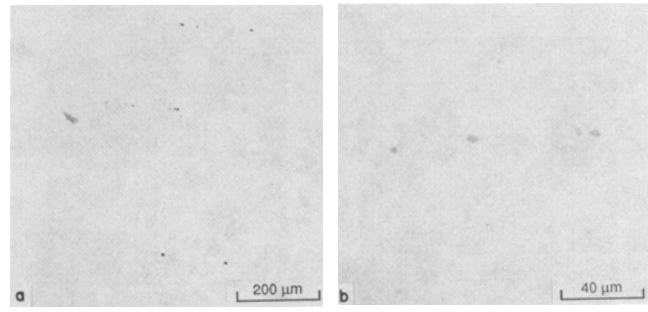

Fig. 4—Micrograph illustrating strings of inclusion particles in rare earth treated AF1410 heat: (*a*) low magnification view of typical spacing in short transverse direction and (*b*) higher magnification view showing shape of individual particles.

$$X_0 = 0.89 \cdot R_0 \cdot f^{-1/3} \qquad \text{where } f = \text{volume fraction}$$

The results of these calculations are presented in Table VI. Note that the average inclusion radius in heat 1 (La treated) was larger (R_0 = 0.64 μm) than that in heat 2 (R_0 = 0.18). This difference in size at nearly the same volume fraction produced more widely spaced inclusions in heat 1 (X_0 = 7.6 μm) compared to heat 2 (X_0 = 2.3 μm).

Two principal types of inclusions were found to exist in the rare earth treated heat, as indicated by energy dispersive analysis of composition. Larger inclusions (2 to 5 μm diameter) exhibited a multi-phase appearance and were found to be of complex composition containing principally La and various small amounts of P, As, and S. These were most likely oxy-sulfides possibly in conjunction with LaP and La_2As. Figure 5(a) shows one of these complex oxy-sulfides along with a representative EDS spectrum. The particles found in the strings were of similar composition but even larger. Smaller particles (0.5 to 2.0 μm diameter) were also present which were found to contain only La and S (see Figure 5(c)). This was consistent with the expected sequence of inclusion formation in rare earth treated steels in which rare earth oxides form first followed by oxy-sulfides, then by sulfides, and then finally by rare earth phosphides and/or arsenides.[8,9] In contrast, the inclusions in heat 2 consisted predominantly of smaller particles (0.1 to 0.8 μm diameter) containing large amounts of Cr and S. No Mn could be detected in these particles. Only a few larger inclusions containing principally Al with small

Table VI. Inclusion Characteristics

Material	f	R_0 (μm)	X_0 (μm)
Heat 1 (La)	0.00042	0.64	7.6
Heat 2	0.00034	0.18	2.3

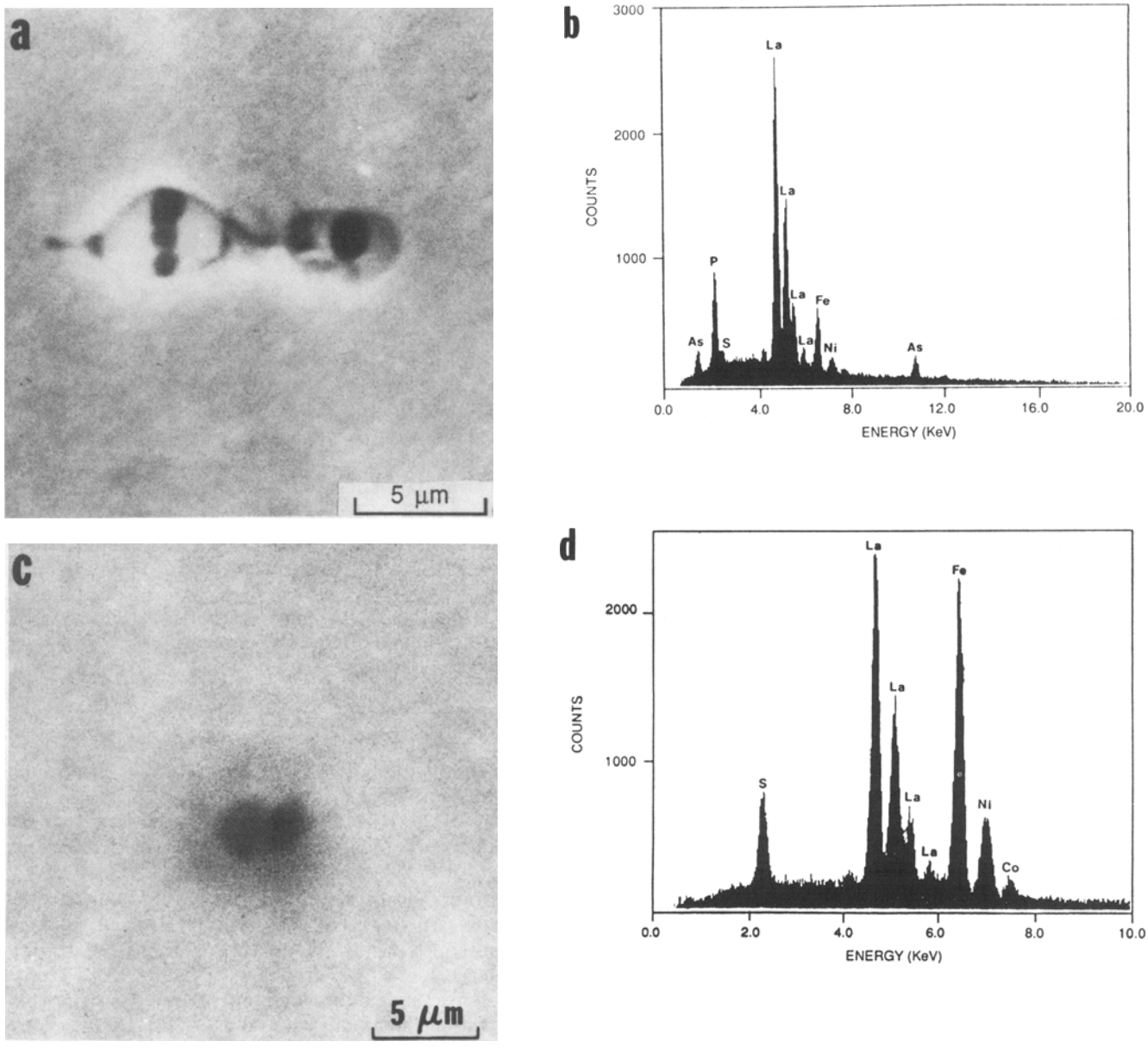

Fig. 5—Typical nonmetallic inclusions in La-treated AF1410 heat. (*a*) Complex particle containing La, P, S, and As. (*b*) EDS spectrum for particle shown in (a). (*c*) Spheroidal lanthanum sulfide. (*d*) EDS spectrum for particle shown in (c).

amounts of calcium were observed, indicating that these particles were most likely complex calcium aluminate deoxidation products. From this information, it was concluded that the smaller particles were sulfides of the Cr_xS_y type, possibly containing small amounts of Mn and/or Fe. This is consistent with the observations of Brammar,[37] who suggested that if the Cr/Mn ratio exceeds 12/1, as it does in heat 2, then Cr_7S_8 may be the predominant sulfide type in lieu of MnS. A typical EDS spectrum of these inclusions is shown in Figure 6.

A comparison was made of the undissolved particles present in each heat after quenching from the austenite region using the carbon extraction replica procedure described earlier. For both heats most of the particles were found to be rich in Mo with smaller and varying amounts of Cr and sometimes Ti, as illustrated in Figure 7. They were identified as hcp M_2C carbides by electron microdiffraction analysis. However, again for both heats, a few particles were found which were rich in titanium and possessed an fcc crystal structure with lattice spacings similar to TiN or TiC. Size distributions were obtained for the particles on the extraction replicas and no significant size difference (95 pct confidence level) between the two heats could be detected. A comparison of the average diameters and estimated volume fractions of these heats is presented in Table VII. Heat 1 exhibited a somewhat higher volume fraction than heat 2, but the difference is well within the accuracy in determining volume fraction by this method.

D. *Fractography and Fracture Surface Particle Characterization*

Low magnification photos of the fracture surfaces of compact tension specimens are presented in Figure 8 for

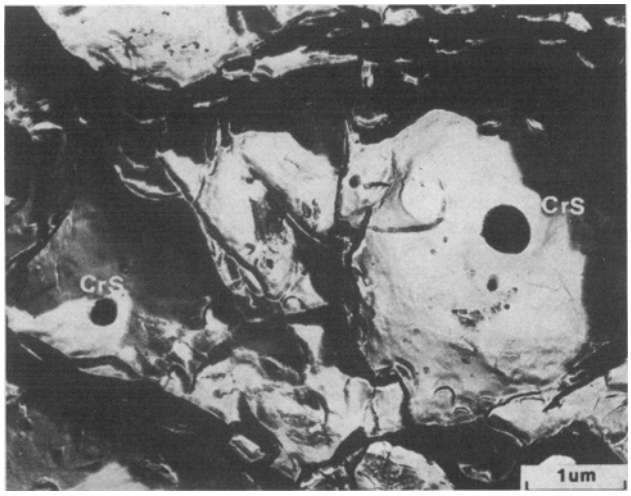

(a)

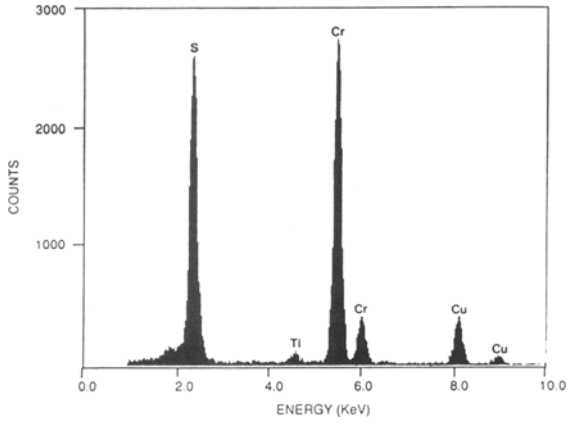

(b)

Fig. 6—(*a*) TEM extraction replica fractograph illustrating chromium sulfides in primary voids of heat 2. (*b*) Representative EDS spectrum for chromium sulfide particles.

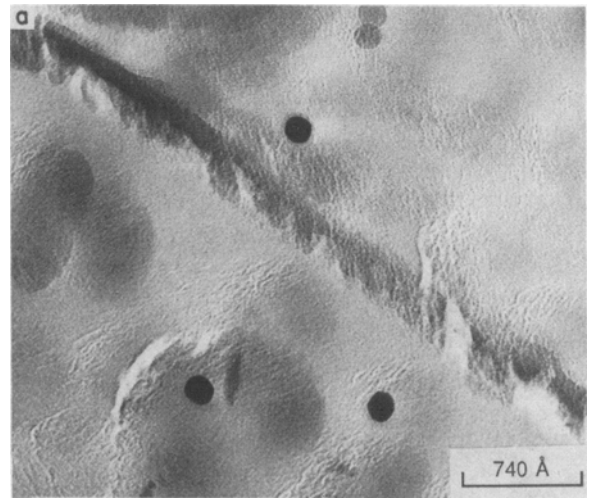

(a)

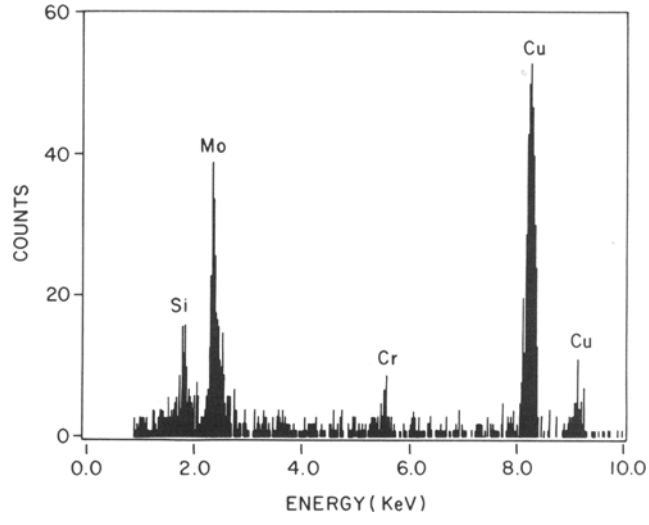

(b)

Fig. 7—High magnification TEM bright-field image from extraction replica of polished cross-section of as-quenched material showing typical undissolved M_2C particles in AF1410 heat 1 and a representative EDS spectrum of these undissolved particles.

each heat and aging treatment. All surfaces exhibited a dull gray, fibrous appearance with no evidence of bright cleavage areas at these magnifications. The difference in toughness level between the two heats can be inferred by comparison of the extents of shear lip formation on the sides of these specimens. For a given aging temperature, a larger shear lip region was apparent for heat 1. Also, note the well-developed periodic lines perpendicular to the crack growth direction present on the fracture surface of heat 1 aged at 510 °C. These lines were very similar in appearance to the "fractographic lines" normally present in maraging steels and previously described by Yoder.[38]

Fracture of J_{IC} specimens of heat 1 occurred entirely by a microvoid coalescence mechanism after aging at 425 °C and at 510 °C (Figures 9(a) and 9(b)). In both cases, the fracture surfaces were covered by two distinct void distributions. One distribution consisted primarily of larger voids, most of which contained inclusion particles resolvable in the SEM. Some of these particles were shattered, indicating void nucleation by a particle fracture mechanism while others were not fractured, indicating nucleation by interface decohesion (Figure 10). As determined by energy dispersive spectroscopy, the shattered particles were normally the complex inclusions, but only La and S could be detected in most of the particles which were not fractured. The secondary void distribution was made up of smaller voids which contained no particles resolvable in the SEM.

Table VII. As-Quenched Polished Surface Carbon Extraction Replica Data

Material	Average Diameter (Å)	Standard Deviation (Å)	Number of Particles	N_s (#/μm^2)	f	X_0 (μm)
Heat 1	251	153	180	5.1	0.0023	0.084
Heat 2	234	170	222	3.3	0.0016	0.089

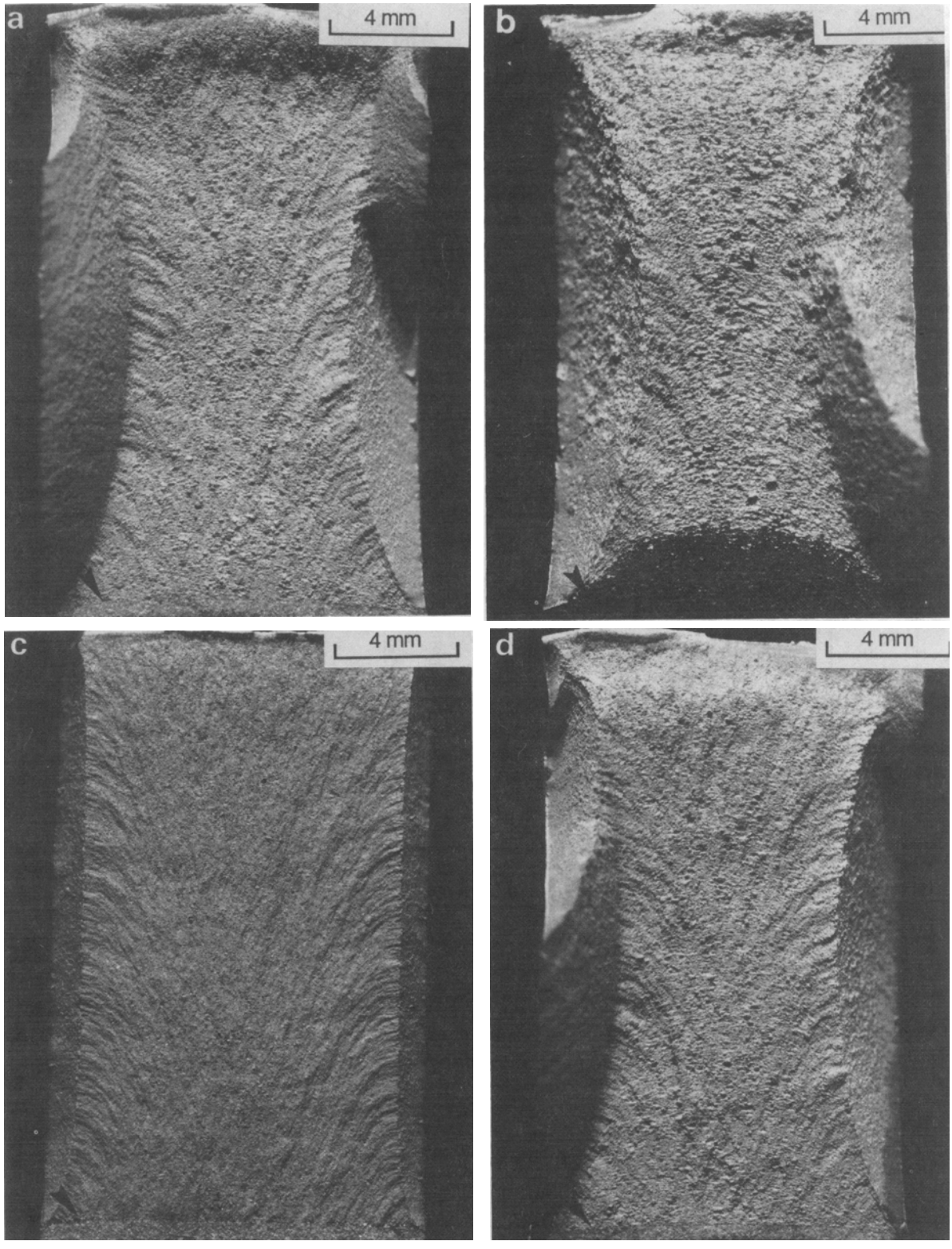

Fig. 8—Low magnification photographs of fractured compact tension specimens of AF1410: (*a*) heat 1, 425 °C; (*b*) heat 1, 510 °C; (*c*) heat 2, 425 °C; (*d*) heat 2, 510 °C.

Qualitatively, the size of the voids associated with the inclusion particles in heat 1, *i.e.*, the primary voids, appeared to increase after aging at 510 °C compared to aging at 425 °C. In addition, the percentage of the fracture surface covered by these primary voids appeared to increase for the 510 °C condition. These qualitative observations were confirmed by quantitative fractographic measurements, as summarized in Table VIII. For heat 1 the average void radius, R_v, of the voids containing inclusions increased from 2.83 μm for aging at 425 °C to 5.52 μm for aging at 510 °C, as

Table VIII. Quantitative Fractographic Information

Condition	R_0^B (μm)	R_0^F (μm)	R_V (μm)	$(R_V/R_I)_{avg}$	$(R_V/R_I)\|_{R_0}$	R_V° (μm)	A_f^{sec}
425 °C							
Heat 1	0.64	0.58	2.83	5.6	4.7	1.10	0.37
Heat 2	0.18	0.19	1.25	7.1	6.7	0.76	0.25
510 °C							
Heat 1	0.64	0.72	5.52	9.2	8.6	1.79	0.12
Heat 2	0.18	0.18	1.65	9.9	9.2	0.81	0.12

R_0^B is average inclusion radius determined from polished cross-sections.
R_0^F is average inclusion radius determined from fracture surfaces.
R_V is the average size of voids containing inclusions.
R_V° is the average size of all voids.
A_f^{sec} is area fraction of secondary voids.

determined from random 1000× SEM fractographs. In addition, the mean radius of all of the voids on the fracture surface increased from 1.10 μm at 425 °C to 1.79 μm at 510 °C. Estimates of the area fraction of inclusion nucleated voids (primary voids) *vs* secondary voids were made for each aging condition, using a point counting approach on representative fractographs. The area fraction of primary voids increased from approximately 0.63 for the 425 °C aging condition to 0.88 for the 510 °C treatment. Inclusion size measurements were made on the inclusions remaining on the fracture surface for each aging treatment. The fracture surface average inclusion radius, R_0^F, was found to be smaller than the bulk inclusion radius, R_0^B, for heat 1 at 425 °C while it was found to be larger for heat 1 at 510 °C. It should be noted that it was very difficult to determine the size of individual particles remaining on the fracture surface of the rare earth treated steel since many of these particles were fractured into numerous pieces, as shown in Figures 9 and 10. The inclusion radii (R_I) of these fractured

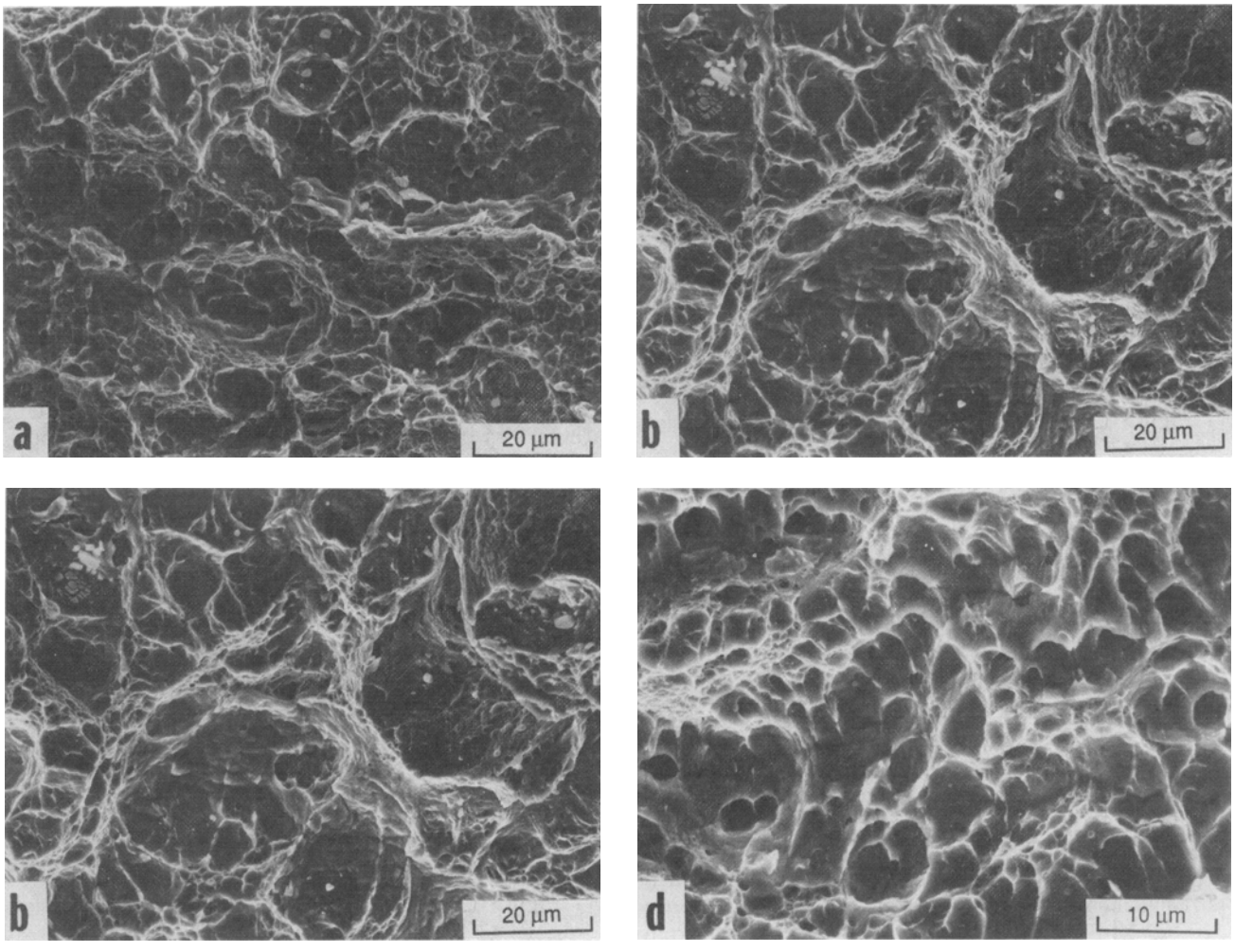

Fig. 9—SEM fractographs near zone of J_{IC} compact tension specimens for (*a*) heat 1, 425 °C; (*b*) heat 1, 510 °C; (*c*) heat 2, 425 °C; (*d*) heat 2, 510 °C.

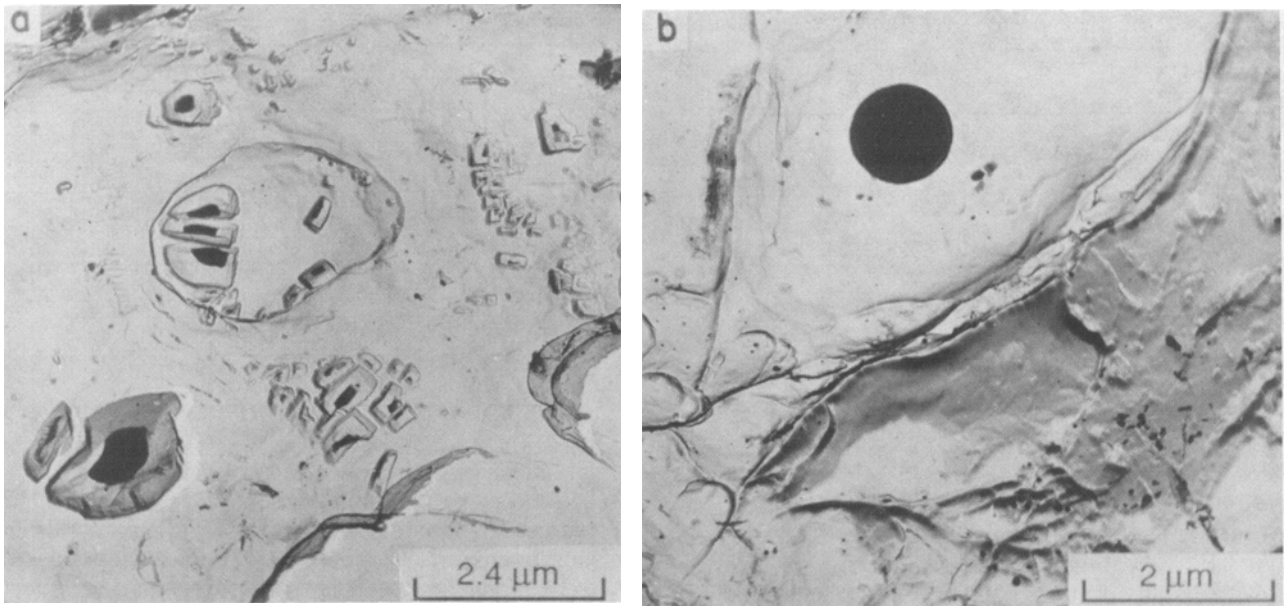

Fig. 10—TEM bright-field micrographs of fracture surface extraction replicas showing (*a*) shattered complex La oxy-sulfide particle and (*b*) a spherical inclusion containing La and S.

particles were estimated by measuring the size of each of the individual pieces of the fractured particles within a given void and assuming that each piece was a sphere and then computing the total volume of these individual pieces. R_I was then taken as the radius of a sphere with volume equivalent to the total volume of the individual pieces. Finally, to characterize the extent of void growth for the inclusion nucleated voids, distributions of R_V/R_I *vs* R_I were obtained. Both the average value of the extent of void growth term, R_V/R_I, and the extent of void growth evaluated at the average inclusion radius ($(R_V/R_I)|_{R_0}$ for heat 1, are reported in Table VIII.

Typical SEM fractographs obtained from compact tension specimens for heat 2 at each aging temperature are presented in Figures 9(c) and (d). Fracture at both aging temperatures occurred principally by the process of microvoid coalescence with two different void size distributions. However, the distributions were not as distinctly different as the void size distributions noted in heat 1. One set of voids consisted of inclusion nucleated voids in which the particles could be resolved in the SEM while the other set again consisted of voids in which no particles could be resolved. The inclusions on the fracture surfaces in heat 2, which were in general much smaller than in heat 1, contained only Cr and S according to their EDS analysis. None of these particles was found to fracture.

As was the case for heat 1, the void sizes on the fracture surfaces of compact tension specimens from heat 2 appeared to increase when the aging temperature was raised from 425 °C to 510 °C and the area fraction of the secondary voids appeared to decrease. Again this was confirmed by measurements of individual inclusion nucleated voids and overall average void sizes obtained from random 2000× SEM fractographs. The results of these measurements are summarized in Table VIII. The average inclusion nucleated void radius increased from 1.25 μm at 425 °C to 1.65 μm at 510 °C and the overall average void size increased from 0.76 μm to 0.81 μm, respectively. These increases in void sizes as the aging temperature was increased from 425 °C to 510 °C were not as dramatic as for heat 1. Also, R_V for heat 2 was considerably smaller than for heat 1 at a given aging treatment. Similarly to heat 1, the area fraction of primary voids increased from 0.75 to 0.88 as the aging temperature was increased from 425 °C to 510 °C. The average fracture surface inclusion size, R_0^F, was very similar to the bulk inclusion radius for both aging temperatures. As for heat 1, R_V/R_I was plotted as a function of R_I for both aging temperatures. Both $(R_V/R_I)_{avg}$ and $(R_V/R_I)|_{R_0}$ increased with aging temperature. Unlike R_V, $(R_V/R_I)|_{R_0}$ was larger for heat 2 at a given aging temperature.

The fracture surfaces of J_{IC} specimens for all four microstructures were predominantly of ductile failure. However, it should be pointed out that J_{IC} specimens of heat 2 aged at 425 °C exhibited isolated areas of intergranular fracture. These regions of intergranular failure could be found only in areas within about 300 μm from the end of the fatigue crack, as illustrated in Figure 11, and covered approximately 5 pct of the area along the thickness direction within this 300 μm strip. No such intergranular regions were found on fracture surfaces of heat 1 aged at 425 °C. In addition, no such intergranular regions were present on the fracture surfaces of the Charpy impact specimens or the plane strain tensile specimens in either heat at any aging treatment. However, intergranular secondary cracks were present in compact tension specimens from both heats of AF1410 aged at 425 °C. These secondary cracks were also present in Charpy impact specimens from both heats after tempering at 425 °C.

In addition to scanning electron fractography, fracture surface extraction replicas of both heats at each aging temperature were prepared and examined in the TEM. The purpose of this work was to identify the void initiating particles present in the secondary voids.

Figure 12 shows the secondary voids on the fracture surface of heat 1 after aging at 425 °C along with the second phase particles residing in them. Two secondary

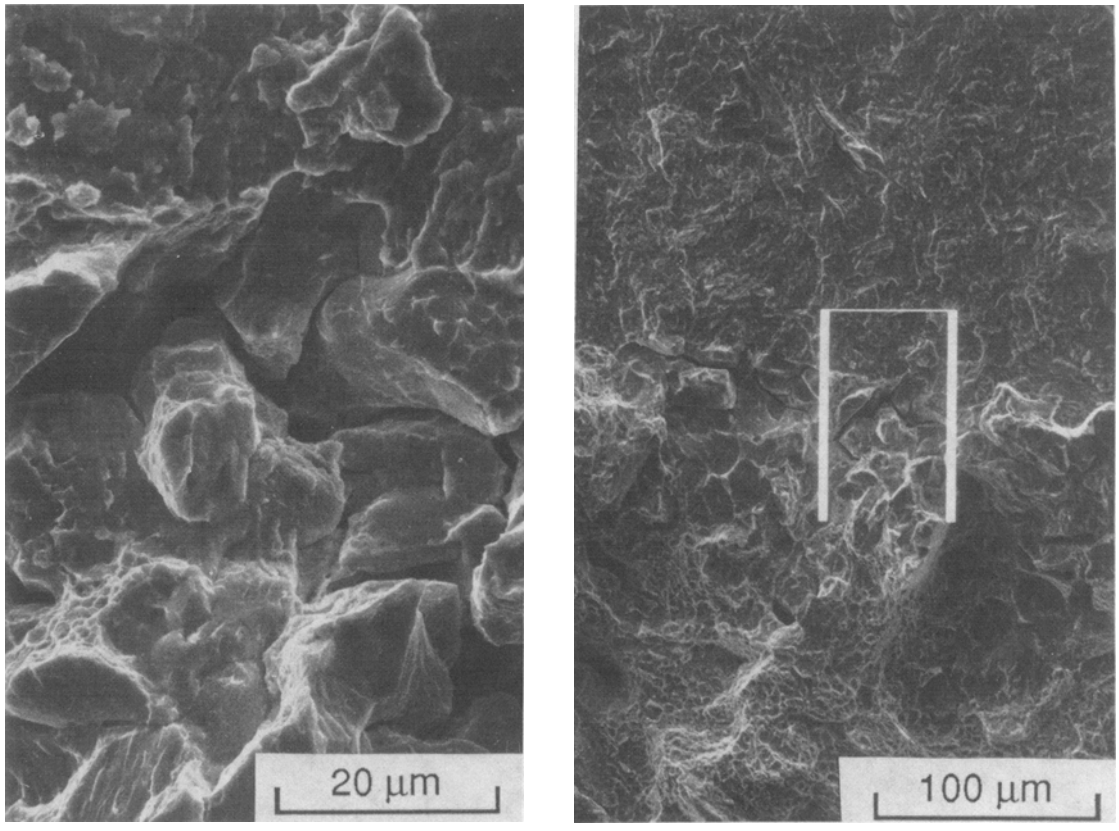

Fig. 11 — SEM fractograph showing region of intergranular fracture near stretch zone of J_{IC} specimen from AF1410 heat 2 aged at 425 °C.

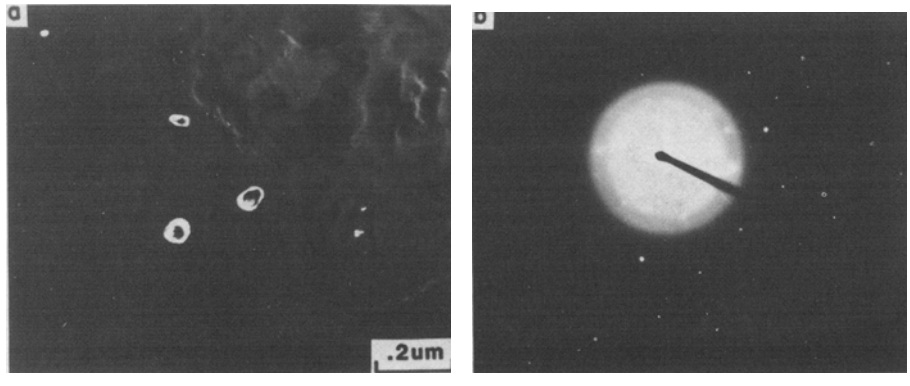

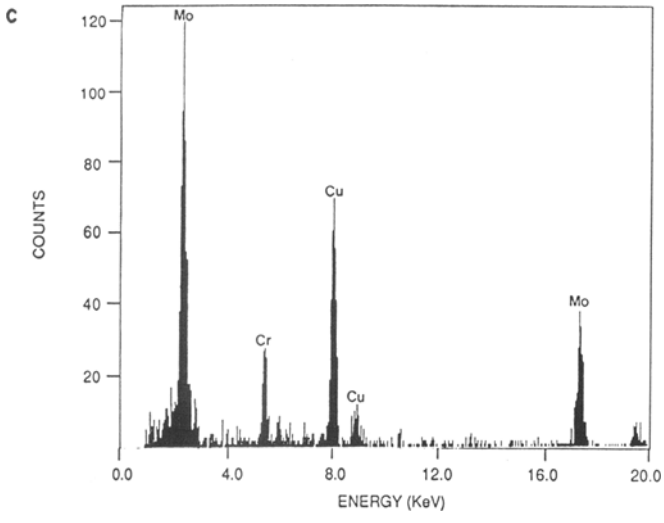

Fig. 12 — TEM bright-field of fracture surface extraction replica of heat 1 aged at 425 °C and an EDS spectrum of a typical M_2C type particle.

particle types were present. Both were found to be of complex composition. Most of the particles contained principally Mo with smaller and varying quantities of Cr and Fe and sometimes Ti. A typical EDS spectrum for these particles is found in Figure 12. These molybdenum-rich particles were found to possess an hcp crystal structure based on analyses of both conventional electron diffraction patterns and microdiffraction patterns. A comparison of lattice plane *d*-spacings from a number of diffra tion patterns yielded good agreement with the lattice spacings of Mo_2C. The second type of particle present after aging heat 1 at 425 °C contained principally Fe with smaller quantities of Mo and Cr. A typical EDS spectrum for such a particle is shown in Figure 13.

Approximately 25 pct of the particles analyzed were found to be iron-rich. These particles are highlighted by arrows in Figure 13. Although diffraction information was not obtained from these particles, their composition was consistent with their being cementite. These particles were in general somewhat larger than the molybdenum-rich particles. The types and relative amounts of the particles in the secondary voids of heat 2 aged at 425 °C were very similar to those described above for heat 1 aged at 425 °C.

After aging at 510 °C the secondary particles found on the fracture surface replicas for heat 1 and heat 2 were similar; therefore, results after aging at 510 °C will be presented only for heat 1. Particles associated with the secondary voids for heat 1 aged at 510 °C are shown in Figure 14. These particles were identified as M_2C by electron diffraction and were found to contain principally Mo with smaller amounts of Cr and Fe. In addition, a few of these particles contained Ti. No Fe-rich particles were found in the secondary voids after aging at 510 °C. However, a few particles were found to be Cr-rich with some Fe present.

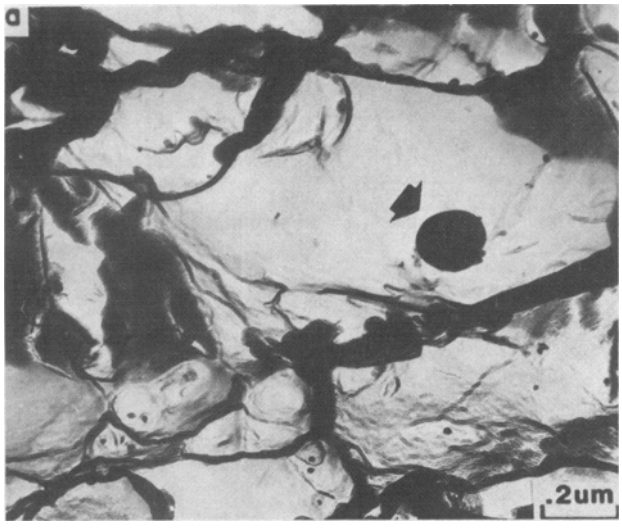

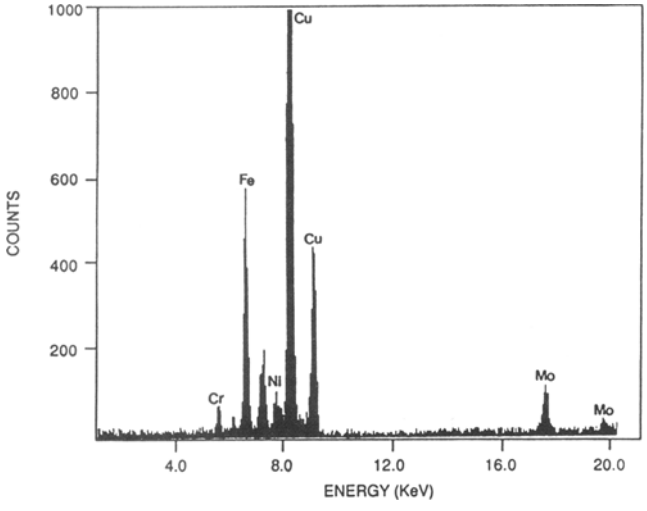

(*b*)

Fig. 13 — TEM bright-field of fracture surface extraction replica of heat 1 aged at 425 °C and an EDS spectrum of the iron-rich particles found on the fracture surfaces of both heats aged at 425 °C.

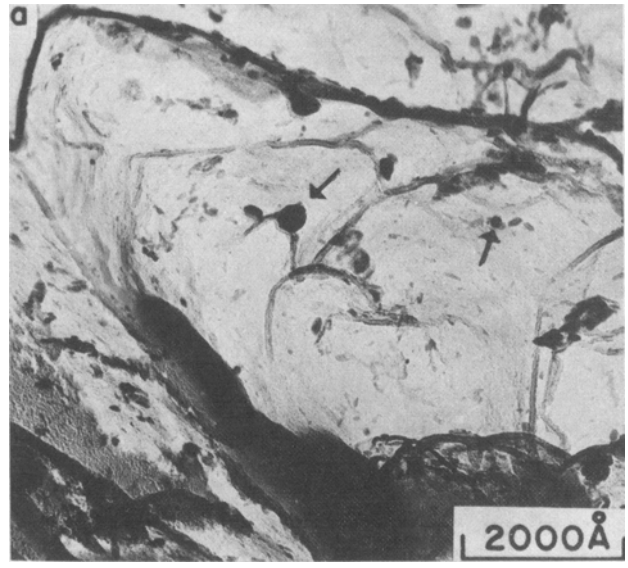

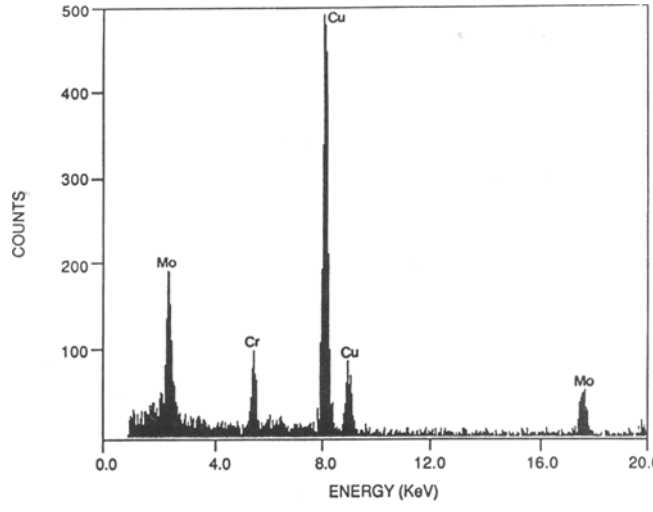

(*b*)

Fig. 14 — TEM bright-field of fracture surface extraction replica of heat 1 aged at 510 °C with an EDS spectrum of the M_2C type particles which were the vastly predominant secondary particle found on fracture surfaces of both heats aged at 510 °C.

The sizes of the secondary particles which were clearly associated with microvoids were measured from random TEM extraction replica fractographs for each heat and aging treatment. Table IX provides a summary of these data

Table IX. Summary of Fracture Surface Carbon Extraction Replica Data

Material	Aging Temperature (°C)	Average Diameter (Å)	Standard Deviation (Å)
Heat 1	425	359	160
Heat 2	425	389	214
Heat 1	510	298	132
Heat 2	510	349	203
Heat 1*	AQ	251	170
Heat 2*	AQ	234	180

*Carbon replica data from polished cross-sections of as-quenched material for comparison.

along with the data from the polished extraction replicas obtained from as-quenched material. The average particle size of secondary particles associated with voids appeared to decrease as the tempering temperature was increased from 425 °C to 510 °C in heat 1 and heat 2. This decrease was found to be significant to a 95 pct confidence level for heat 1 based on a two-sample comparison of means analysis using the F-test followed by t-test. However, the difference for heat 2 was not found to be significantly different to a 95 pct confidence level.

In summary, the particles extracted from secondary voids were similar for both heats at a given aging temperature, in terms of both type and size. After aging at 425 °C, approximately 75 pct of the secondary particles were M_2C type particles and approximately 25 pct were Fe-rich particles believed to be cementite. After aging at 510 °C the secondary particles were almost entirely M_2C type particles with a very small percentage of particles rich in Cr and some Fe present.

IV. DISCUSSION

The mechanical properties have been determined at two aging temperatures for two heats of AF1410 steel. The heats differed essentially only in inclusion type. It was found that at a given aging temperature the fracture initiation toughness was strongly dependent on inclusion type. Further, it was found that for a given inclusion type the toughness was also dependent on aging temperature. In this discussion we will consider fracture initiation toughness and address three topics: the role of inclusion type, the role of aging temperature, and attempts to model fracture initiation which incorporate inclusion characteristics as well as other aspects of the microstructure. Finally these results will be compared to an earlier study of a La modified heat of AF1410 steel.

A. *Role of Inclusion Type*

For a given aging treatment the results show that changing inclusion type at a reasonably constant volume fraction had no influence on the smooth axisymmetric or the plane strain tensile ductilities. However, at a fixed aging temperature, the inclusion type had significant influence on fracture initiation toughness, as shown in Table IV. It is difficult to ascribe this effect to anything except the characteristics of the inclusions. For example, the two steels had the same prior austenite grain size and the same type of undissolved particles inherited from the austenitizing temperature. Further, these undissolved particles had almost the same average size and spacing as shown in Table VII. Given the very similar compositions of the two heats, it seems reasonable to assume that the microstructures developed at a given aging temperature were very similar for the two heats. For example, the retained austenite levels for the two heats are almost identical at a given aging temperature.

The most plausible explanations for the effect of inclusion type on the fracture initiation toughness would appear to be either the observed difference in inclusion spacing, differences in nucleation strain, or possibly a combination of both effects. It is normally assumed that inclusions such as MnS are weakly bonded to the matrix and can be regarded as pre-existing voids. However, it has been suggested that the CrS inclusions contained in heat 2 may be more strongly bonded to the matrix than MnS.[39] In addition, no one has yet addressed the issue of the nucleation strain for lanthanum oxy-sulfides or lanthanum oxides, the inclusions in heat 1. However, given that the smooth axisymmetric tensile ductilities are the same for both heats at a given aging temperature, it is suggested that the nucleation strains for the inclusions in both heats are at least comparable. This is based on our conclusion that at a given aging temperature the microstructures achieved for the two heats are almost identical and that the void growth equations of Rice and Tracey[40] suggest that for otherwise identical microstructures, differences in nucleation strain should result in changes in the smoother axisymmetric tensile ductility.

If it is accepted that nucleation strains associated with the two inclusion distributions are comparable, then it would seem reasonable to conclude that the improved toughness of the La modified heat is primarily due to the increase in the inclusion spacing. The inclusion spacing for the lanthanum modified heat is 7.62 μm compared to 2.3 μm for the chromium sulfides in heat 2. This increased inclusion spacing is entirely due to an increase in the average inclusion size as the inclusion volume fraction is actually slightly higher for the La modified heat. This conclusion is consistent with work on low alloy steels where increasing the manganese sulfide spacing at a reasonably constant inclusion volume fraction by increasing the average sulfide size resulted in a significant improvement in toughness. The influence of inclusion type on the toughness of AF1410 at a given aging temperature is reflected in the ratio of the δ_{IC} values associated with the two inclusion types (δ_{IC} (heat 1)/δ_{IC} (heat 2)), as shown in Table X. These ratios are almost identical to the ratio obtained for the series of low alloy steels[3] where the inclusion spacing (MnS) was increased from 3.5 μm to 10 μm. It is suggested that this comparison supports our conclusion that the nucleation strains for the inclusions in heat 1 and the CrS in heat 2 are comparable; that is, these results are similar in magnitude to those obtained by increasing the size and spacing of a fixed inclusion type, MnS, believed to be very weakly bonded to the matrix.

Table X. Comparison of Effects of X_0 on δ_{IC}

Material	R_0 (μm)	X_0 (μm)	δ_{IC} (μm)	$\delta_{IC_1}/\delta_{IC_2}$
AF1410–425 °C				
Heat 1	0.64	7.6	23	1.92
Heat 2	0.18	2.3	12	
AF1410–510 °C				
Heat 1	0.64	7.6	66	2.35
Heat 2	0.18	2.3	28	
Low Alloy Steels				
Heat 1	0.72	9.8	20	2.33
Heat 2	0.28	3.5	8.6	

Note: The data for the low alloy steels are from Reference 3. The data for heat 2 are the average for the base, base + Ni, and base + Si steels, and the data for heat 1 are for the base + Ni + Si steel. The inclusions in the low alloy steels were MnS.

B. *Fine-Scale Microstructure*

For a given inclusion type changing the microstructure by increasing the aging temperature from 425 °C to 510 °C resulted in an increase in both the smooth axisymmetric and plane strain tensile ductility, a decrease in work hardening exponent, and an increase in the fracture initiation toughness. The microstructure can influence the fracture process both directly and indirectly. It can influence the fracture process directly by providing particles which may actually nucleate secondary voids. It can also indirectly influence the fracture through the flow properties which can influence void nucleation, void growth, and the crack tip blunting characteristics.[41,42,43]

These results suggest that the improvements in ductilities and fracture initiation toughness associated with the increase in aging temperature for a fixed inclusion type are at least partly due to changes in the particles precipitated on aging. Examination of the fracture surfaces of both heats of AF1410 aged at 425 °C suggests that the majority (≈75 pct) of the secondary voids were nucleated by M_2C type particles inherited from the austenitizing treatment. The other secondary voids (≈25 pct) appear to be nucleated at particles formed on aging. These particles were not present in the as-quenched condition and contained Fe with smaller amounts of Cr and Mo.

On aging at 510 °C it was found again that principal secondary void initiating particles were M_2C particles inherited from the austenitizing temperature. On aging at 510 °C there is on the fracture surface no evidence of the Fe-rich particles observed at 425 °C. Nor is there any evidence that the fine intralath M_2C particles precipitated on aging at 510 °C were nucleation sites for secondary voids. A few Cr-rich particles, containing small amounts of molybdenum, were observed to nucleate voids on aging at 510 °C. These particles are assumed to have formed on tempering as they were not observed in the as-quenched condition. Thus it appears that for both aging temperatures most of the secondary voids were nucleated at M_2C particles inherited from the austenitizing temperature. The difference appears to be that on aging at 425 °C about 25 pct of the secondary voids are nucleated at particles precipitated on aging, while on aging at 510 °C this percentage is very much less.

Speich *et al.*[4] suggested that the low toughness associated with aging at 425 °C in HY180 steel was due to the presence of large intralath cementite particles. As expected from the work of Speich *et al.*,[4] large intralath cementite particles are observed in AF1410 aged at 425 °C.[7] However, it is not clear that these intralath particles are the only particles formed on tempering which could nucleate secondary voids. It is possible that particles precipitated at 425 °C and which nucleate voids could also be interlath carbides resulting from the decomposition of retained austenite. As shown in Figure 3, AF1410 retained austenite decomposition is almost complete on aging at 425 °C.

These observations appear to be consistent with the increase in the extent of void growth ($(R_V/R_I)|_{R_0}$) and the decrease in the area fraction of secondary voids associated with the increase in aging temperature from 425 °C to 510 °C for a given inclusion type. For heat 1 (La treated) $(R_V/R_I)|_{R_0}$ increased from 4.7 to 8.6 and for heat 2 (CrS inclusions) this quantity increased from 6.7 to 9.2. We note that the extent of void growth at a given aging temperature is less for the larger inclusions. This is consistent with results observed for low alloy steels containing large and small MnS particles at a fixed volume fraction.

These results suggest that there is a direct effect of aging on the fracture process. That is, on aging at 425 °C particles are precipitated which are much more favorably disposed to the nucleation of secondary voids than the particles precipitated on aging at 510 °C. It may be, as will be discussed, that microstructural changes caused by increasing the aging tempering temperature could also indirectly influence the fracture process.[41,44]

C. *Modeling Fracture Behavior*

It has been proposed[45] and found to be the case for many materials[3,7,10,46,47] that δ_{IC} scales as $X_0(R_V/R_I)|_{R_0}$. δ_{IC} is plotted in Figure 15 as a function of $X_0(R_V/R_I)|_{R_0}$ for the two heats and two aging temperatures investigated here. The behaviors for these microstructures are roughly consistent with the linear relationship between δ_{IC} and $X_0(R_V/R_I)I_{R_0}$ observed for previously investigated materials. The microstructures achieved after aging at 425 °C exhibit behavior which parallels the correlation observed for other materials. However, the microstructures obtained after aging at 510 °C deviate from the linear relationship between δ_{IC} and $X_0(R_V/R_I)|_{R_0}$. On aging at 510 °C, δ_{IC} is 16 μm (heat 2) and 25 μm (heat 1), greater than would be expected from this correlation. Why the 510 °C microstructure departs from this correlation is not known. Several factors may be suggested to cause a departure from this linear relationship. First, it is possible δ_{IC} is no longer linear in X_0; however, if the only problem is δ_{IC} no longer linear in X_0, then $X_0(R_V/R_I)|_{R_0}$ would lead to an overestimate of δ_{IC}, not the underestimate observed here. Implicit in the proposal that $\delta_{IC} \approx X_0(R_V/R_I)$ are the assumptions that single particle nucleated voids coalesce with the crack tip and that the rate of void growth with δ is a constant. It is possible that for very ductile materials, the voids which coalesce with the crack tip are not single particle nucleated voids. In addition, blunting to vertices would be expected to lead to void

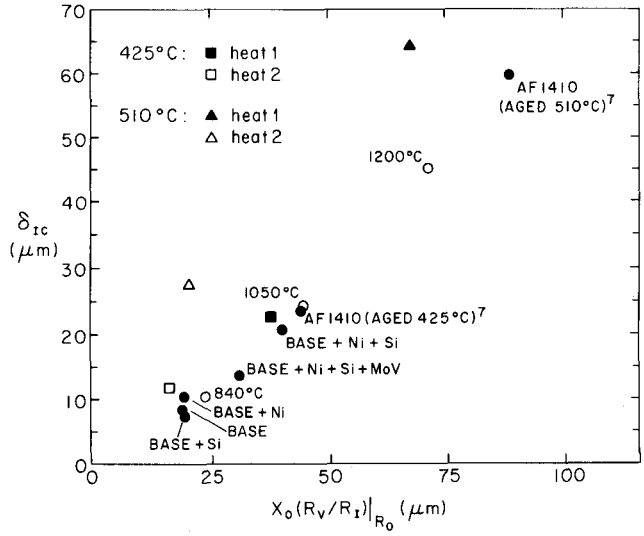

Fig. 15—δ_{IC} plotted as a function $X_0(R_V/R_I)|_{R_0}$ for the four microstructures investigated here, for an earlier heat of La modified AF1410[7] and other ultra high-strength steels.[3,46,47]

growth rates which are different than for smooth blunting.[41,42] Available results[43,44] suggest that as long as the plane strain tensile ductility is not too great and smooth blunting is obtained, the correlation $\delta_{IC} \approx X_0(R_V/R_I)|_{R_0}$ holds; in fact, this was shown to be true for materials for which the plane strain tensile ductility is as high as 0.25.[44] Given that the plane strain tensile ductility of AF1410 aged at 510 °C is less than 0.25, it is very likely that blunting to vertices will be observed after aging at this temperature. That HY180 aged at 510 °C blunts to vertices[50] further suggests that this will occur in AF1410 aged.

D. *Comparison of Heats of La Treated AF1410*

The fracture behavior of another La modified heat of AF1410 was discussed in a previous paper.[7] A conclusion of that work was that the high fracture toughness of La modified AF1410 steel aged at 510 °C was largely the result of the large inclusion spacing. This seems to be verified by the work reported here. In fact, the K_{IC} predicted for AF1410 aged at 510 °C at a small inclusion spacing is very close to that measured for the CrS heat. In addition, it was predicted that the extent of void growth for the heat with the smaller, more closely spaced inclusions would be greater than for the larger, more widely spaced inclusions in the La modified AF1410. This is also verified by this work.

However, in two respects the behavior of the La modified heat of AF1410 studied here and the one studied earlier are different. First, the heat studied here had a higher fracture initiation toughness (δ_{IC} = 66 μm) than the earlier heat (δ_{IC} = 61 μm), even though X_0 for this heat was smaller (7.62 μm compared to 10.4 μm). Second, on aging at 510 °C the behavior of the earlier heat was more consistent with the linear relationship between δ_{IC} and $X_0(R_V/R_I)I_{R_0}$.

The lower toughness of the earlier heat, despite a larger X_0, could be due to its containing a more detrimental distribution of undissolved carbides inherited from the austenitizing temperature. The plane strain tensile ductility appears sensitive to differences in undissolved particle dispersions.[44] As shown in Table XI, the effective plane strain tensile ductility and the extent of void growth ($(R_V/R_I)|_{R_0}$ are slightly less for the earlier heat of AF1410. However, these differences seem too small to account for a marked reduction in fracture initiation toughness.

The seemingly unexpectedly low toughness of the earlier material is probably associated with the nonlinearity of the relationship between toughness (δ_{IC}) and X_0. Given the accuracy of measurements, the curve drawn for δ_{IC} as a function of X_0 in Figure 16 is probably reasonable. This curve suggests that for this microstructure δ_{IC} will increase very slowly with X_0 for inclusion spacings greater than about 10 μm. When this curve is extended to the plot of δ_{IC} *vs* $X_0(R_V/R_I)|_{R_0}$ (Figure 17), it can be deduced that the linear relationship between δ_{IC} and $X_0(R_V/R_I)|_{R_0}$ observed for the first heat is only fortuitous.

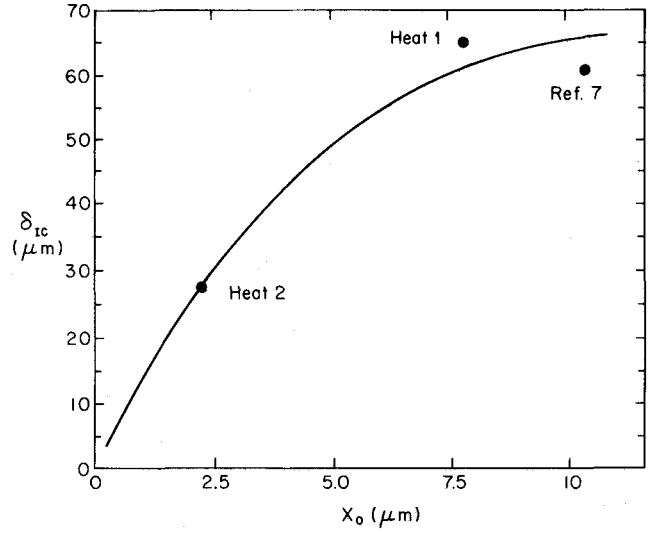

Fig. 16—δ_{IC} plotted as a function of X_0 for the 510 °C microstructure.

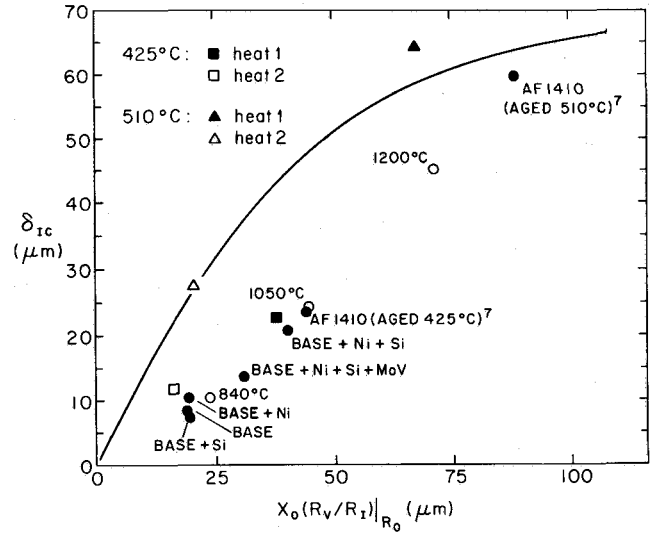

Fig. 17—δ_{IC} plotted as a function of $X_0(R_V/R_I)|_{R_0}$. The curve representing the AF1410 heats aged at 510 °C intersects the linear behavior exhibited by the materials at an X_0 of about 10 to 12 μm.

V. SUMMARY AND CONCLUSIONS

1. The smooth axisymmetric and plane strain tensile properties, Charpy impact toughness, and the fracture

Table XI. Comparison of Lanthanum Treated Heats

Condition	f	R_0^F (μm)	R_0^B (μm)	X_0 (μm)	$(R_V/R_I)|_{R_0}$	δ_{IC} (μm)	$\bar{\varepsilon}_f^{PS}$
425 °C							
This study	0.00042	0.58	0.64	7.6	4.7	28	0.15
Reference 7	0.00036	0.86	0.98	10.4	4.3	26	—
510 °C							
This study	0.00042	0.72	0.64	7.6	8.6	66	0.23
Reference 7	0.00036	0.81	0.98	10.4	8.5	61	0.22

initiation toughness have been measured for two heats of AF1410 steel for aging temperatures of 425 °C and 510 °C. One heat was modified by a La addition and the other was not.

2. The mechanical properties are influenced markedly by increasing the aging temperature from 425 °C to 510 °C. While the strength level does not change appreciably, increasing the aging temperature increases the smooth axisymmetric and plane strain tensile strains to fracture, reduces the work hardening exponent, and increases both the Charpy impact and fracture initiation toughnesses.
3. Of the mechanical properties listed above, only the fracture initiation toughness and the Charpy impact toughness (after aging at 510 °C) were influenced by melt practice. Both of these quantities were higher for the La modified heat.
4. The inclusions in the La modified heat consisted of particles rich in La and S and more complex particles containing La, S, P, and in some cases As. The volume fractions, R_0 and X_0, were 0.00042, 0.64 μm, and 7.6 μm, respectively. The inclusions in the second heat contained Cr and S. For the second heat the volume fractions, R_0 and X_0, were 0.00035, 0.18 μm, and 2.3 μm, respectively.
5. The undissolved carbides in both heats appeared to be primarily M_2C type carbides of almost an identical volume fraction, average size, and spacing.
6. Studies of fracture surface replicas show for both heats that on aging at 425 °C 75 pct of the secondary voids were nucleated at particles inherited from the austenitizing treatment and 25 pct were nucleated at particles precipitated on aging. On aging at 510 °C almost all of the secondary voids were nucleated at particles inherited from the austenitizing temperature.
7. The above direct influence of aging temperature on particles which nucleate voids is consistent with an increase in the extent of growth of voids nucleated at inclusions and the decrease in the area fraction of secondary voids as the aging temperature was increased from 425 °C to 510 °C.
8. While the extent of void growth $(R_V/R_I)|_{R_0}$ increased with aging temperature for both heats, the extent of void growth at a given aging temperature was always greater for the smaller inclusions. The values of $(R_V/R_I)|_{R_0}$ after aging at 425 °C were 4.7 and 6.7 for heats 1 and 2, respectively. The values after aging at 510 °C were 8.6 and 9.2 for heats 1 and 2, respectively.
9. The improvement in δ_{IC} achieved by the lanthanum additions for a fixed fine-scale microstructure (*i.e.*, for a given aging temperature) was attributed to the more than threefold increase in inclusion spacing.
10. It was observed that on aging at 510 °C neither heat exhibited behavior consistent with the linear relationship between δ_{IC} and $X_0(R_V/R_I)|_{R_0}$ observed for previously investigated materials and these two heats aged at 425 °C. It is suggested that this is associated with blunting to vertices.

ACKNOWLEDGMENTS

The authors gratefully acknowledge the financial support of Ellwood City Forge Corporation and of the Army Research Office under contract DAAL03-86-K-0124. In addition, the authors would like to thank Mr. H. L. Black of Cytemp and Dr. J. Moyer of Teledyne-Allvac for the preparation and donation of materials.

REFERENCES

1. J. R. Rice and M. A. Johnson: in *Inelastic Behavior of Solids*, M. F. Kanninen, W. G. Adler, A. R. Rosenfield, and R. J. Jaffee, eds., McGraw-Hill, New York, NY, 1970, pp. 641-72.
2. A. J. Birkle, R. P. Wei, and G. E. Pellissier: *Trans. of ASM*, 1966, vol. 59, pp. 981-90.
3. W. M. Garrison, Jr.: *Metall. Trans. A*, 1986, vol. 17A, pp. 669-78.
4. G. R. Speich, D. S. Dabkowski, and L. F. Porter: *Metall. Trans.*, 1973, vol. 4, pp. 303-15.
5. G. D. Little and P. M. Machmeier: AFML-TR-75-148, Final Report Mar. 1973-Feb. 1975, Air Force Materials Lab., Wright-Patterson Air Force Base, Dayton, OH, 1975.
6. H. L. Black, J. L. Milavec, and R. R. Shiring: Technical Report AFML-TR-79-4181, Air Force Materials Laboratory, Wright-Patterson, OH, 1979.
7. W. M. Garrison, Jr. and N. R. Moody: *Metall. Trans. A*, 1987, vol. 18A, pp. 1257-63.
8. D. A. Kay, W-K. Lu, and A. McLean: *Sulfides in Steel*, ASM, Metal Park, OH, 1975, pp. 23-43.
9. M. P. Seah, P. J. Spencer, and E. D. Hondros: *Metal Science*, 1979, vol. 13, pp. 307-14.
10. W. M. Garrison, Jr.: *Proceedings of the Earl R. Parker Symposium on Structure Property Relationships*, S. D. Antolovich, R. O. Ritchie, and W. W. Gerberich, eds., TMS-AIME, 1985, p. 187.
11. K. J. Handerhan and W. M. Garrison, Jr.: *Scripta Metall.*, 1988, vol. 22, pp. 409-12.
12. AMS 6427, "Aerospace Materials Specification," issued 7-15-80, SAE, Inc., Warrendale, PA.
13. ASTM E8-81, *1983 Annual Book of ASTM Standards*, ASTM, Phila., PA, 1983, p. 197.
14. ASTM E646-78, *1983 Annual Book of ASTM Standards*, ASTM, Phila., PA, 1983, p. 755.
15. D. A. Corrigan, R. E. Travis, V. P. Ardito, and C. M. Adams, Jr.: *Welding Research Supplement*, March 1962, pp. 123s-128s.
16. D. P. Clausing: *Int. J. of Fract. Mech.*, 1970, vol. 6, pp. 71-85.
17. D. P. Clausing: U.S. Steel Report No. 35.066-001 (2), Aug. 1, 1972.
18. J. M. Barsom and J. V. Pellegrino: *Eng. Fract. Mech.*, 1973, vol. 5, pp. 209-21.
19. L. Anand and W. A. Spitzig: *J. Mech. Phys. Solids*, 1980, vol. 28, pp. 113-28.
20. V. Tvergaard, A. Needleman, and K. K. Lo: *J. Mech. Phys. Solids*, 1981, vol. 29, pp. 115-42.
21. ASTM E23-72, *1983 Annual Book of ASTM Standards*, ASTM, Phila., PA, 1983, p. 115.
22. ASTM E813-81, *1983 Annual Book of ASTM Standards*, ASTM, Phila., PA, 1983, pp. 762-80.
23. G. A. Clarke, W. R. Andrews, P. C. Paris, and D. W. Schmidt: ASTM STP 590, ASTM, 1976, pp. 27-42.
24. A. Saxena and S. J. Hudak: *Int. J. of Fract.*, 1978, vol. 14, pp. 453-68.
25. J. G. Merkle and H. T. Corten: Trans. ASME, Vol. 96, Series J, *J. of Pressure Vessel Technology*, 1974, pp. 286-92.
26. *Metals Handbook*, vol. 8, *Metallography, Structures and Phase Diagrams*, ASM, Metals Park, OH, 1973.
27. ASTM E112-81, *1983 Annual Book of ASTM Standards*, ASTM, Phila., PA, 1983, p. 62.
28. B. L. Averbach and M. Cohen: *Trans. AIME*, 1948, vol. 176, pp. 401-14.
29. R. L. Miller: *Trans. AIME*, 1964, vol. 57, pp. 892-99.
30. W. E. Stumpf and C. M. Sellars: *Metallography*, 1968, vol. 1, pp. 25-34.
31. M. F. Ashby and R. Ebeling: *Trans. AIME*, 1966, vol. 236, pp. 1396-1404.
32. *Aerospace Structural Metals Handbook*, 1980 ed., D. J. Maykuth, ed., Battelle Columbus Laboratories, Columbus, OH.
33. G. R. Speich and W. A. Spitzig: *Metall. Trans. A*, 1982, vol. 13A, pp. 2239-58.
34. R. H. Wagoner: *Metall. Trans. A*, 1980, vol. 11A, pp. 165-75.
35. P. H. Salmon-Cox, B. G. Reisdorf, and G. E. Pellisier: *Trans. AIME*, 1967, vol. 239, pp. 1809-17.

36. J. E. Hilliard: *Stereology: Principles and Practices,* Northwestern University, 1981.
37. I. S. Brammar: *J. I. S. I.,* 1963, vol. 201, pp. 752-62.
38. G. R. Yoder: *Metall. Trans.,* 1972, vol. 3, pp. 1851-59.
39. C. J. Middleton: *Metal Science,* 1981, vol. 15, pp. 154-67.
40. J. R. Rice and D. M. Tracey: *J. Mech. Phys. Solids,* 1969, vol. 17, pp. 201-17.
41. R. M. McMeeking: *J. of Eng. Mat. and Tech.,* Oct. 1977, pp. 290-97.
42. R. M. McMeeking: *J. Mech. Phys. Solids,* 1977, vol. 25, pp. 357-81.
43. K. J. Handerhan and W. M. Garrison, Jr.: *Scripta Metall.,* 1988, vol. 22, pp. 607-10.
44. K. J. Handerhan: Ph.D. Thesis, Carnegie Mellon University, Sept. 1987.
45. W. M. Garrison, Jr.: *Scripta Metall.,* 1984, vol. 18, pp. 583-86.
46. K.J. Handerhan and W.M. Garrison, Jr.: *Metall. Trans. A,* 1988, vol. 19A, pp. 2989-3004.
47. W. M. Garrison, Jr.: *Scripta Metall.,* 1986, vol. 20, pp. 633-36.
48. C. F. Shih: *J. Mech. Phys. Solids,* 1981, vol. 29, pp. 305-30.
49. B. de Miramon: M. S. Thesis, University of California, Berkeley, CA, 1967 (Lawrence Berkeley Laboratory Report-UCRL-17849).
50. J. Maloney: unpublished research, Carnegie Mellon University, 1987.